Reduction of Injection Voltage in Signal Injection Sensorless Drives Using Capacitor-Integrated Inverter

Yong-Cheol Kwon and Seung-Ki Sul
Department of Electrical and Computer Engineering
Seoul National University
Seoul, Korea
dydcjfe@gmail.com, sulsk@plaza.snu.ac.kr

***Abstract*—In signal injection sensorless drives, the injection voltage can't be reduced under a certain value. The lower limit of the injection voltage mainly comes from the inverter nonlinearity that distorts the injection voltage and degrades the position estimation performance. After analyzing the inverter nonlinearity during the voltage injection, it is revealed that the parasitic capacitances of IGBT switches have a positive effect on sensorless control. Based on this analysis, this paper proposes a method to reduce the injection voltage by connecting additional capacitors to the inverter output. Simulation and experimental results are provided to verify the effectiveness of the proposed idea. In the experiment, using the capacitor-integrated inverter, the injection voltage can be reduced to less than a half without degrading sensorless control performance.**

Keywords—Signal injection sensorless control, inverter nonlinearity, parasitic capcitance.

I. INTRODUCTION

Sensorless control techniques of AC machines have been developed to cope with many concerns related with position sensors such as increased volume and cost of drive system, electromagnetic interference, and reliability issues associated with sensor itself. Especially for sensorless drive at standstill and low speed, high frequency (HF) signal injection based methods [1]-[7] have been widely used in many industrial applications.

Most of the conventional signal injection sensorless methods [1]-[7] utilize the inductance saliency. Since the inductances seen from the terminals of an Interior permanent magnet synchronous machine (IPMSM) are clearly determined by the rotor position, it can be estimated by injecting additional HF voltage signal and analyzing its resultant HF current ripple. In case of surface mounted permanent magnet synchronous machines (SMPMSMs) where d- and q-axes of the rotor are geometrically symmetrical, saturation-induced inductance saliency [4] or eddy-current-reflected resistance saliency [5] can be used.

Conventional sensorless control methods can also be classified according to the type of the injection voltage. Ref. [1] used discrete voltage signal, Ref. [2] used continuous rotating voltage signal in the stationary reference frame, and Ref. [3]-[7] used continuous pulsating voltage signal in the estimated rotor reference frame. In [6]-[7], square-wave injection methods which exhibit excellent dynamic performance were used. Increasing the injection frequency to half the PWM switching frequency [6] or to PWM switching frequency [7] made it possible to increase overall control bandwidths.

However, additional signal injection causes undesired effects such as acoustic noise, reduced voltage margin of inverter output, and HF losses coming from HF excitation of the motor. These problems can be relieved by reducing the magnitude of the injection voltage. But with less injection voltage, the inverter nonlinearity [8]-[14] tends to be more influential and sensorless control performance can be severely degraded. For this reason, the magnitude of the injection voltage should be larger than a certain limit.

There have been many researches on the inverter nonlinearity effects for general AC drives [8]-[14]. In the early literatures [8]-[11], the inverter nonlinearity induced by zero current clamping (ZCC) [8]-[9], parasitic capacitances [10], and dead time and voltage drop across semiconductor devices [11] were analyzed. The inverter nonlinearity can be compensated by adding a compensation voltage to the voltage reference [9] or advancing/delaying the switching instant [10]-[11]. The compensation can also be accomplished using closed-loop disturbance observer [12], look-up table (LUT) [13], or online-adjusted trapezoidal voltage [14]. Thanks to the previous works, the inverter nonlinearity compensation performances are now satisfactory in most applications.

However, the compensation of the inverter nonlinearity becomes more challenging under the signal injection sensorless operation. Since the HF current ripple induced by the voltage injection frequently crosses zero, it is very difficult to accurately estimate the voltage error in the inverter output [15]-[16]. To solve this problem, Ref. [17] proposed a compensation technique which separately estimates HF component of the voltage error and adds it to the voltage reference. In the case of the square-wave injection, which would be the most difficult condition for the inverter nonlinearity compensation, Ref. [18] improved sensorless control performance by regulating HF current ripple.

This paper provides a different approach to attenuate the voltage error induced by the inverter nonlinearity under signal injection sensorless drives, which would finally lead to the reduction of the injection voltage. It is revealed that the inherent parasitic capacitors of IGBTs reduce the voltage error under the signal injection. Although this analysis is developed based on the square-wave injection methods, it is valid for any signal injection sensorless methods [1]-[7]. From this analysis, a capacitor-integrated inverter where additional capacitors are connected to its output terminals is proposed. Using the proposed method, the injection voltage can be reduced without degrading the performance of the sensorless control. Experimental and simulation results are provided to demonstrate the validity of the proposed idea.

II. SIGNAL INJECTION SENSORLESS CONTROL

Fig. 1 shows a typical control block diagram of square-wave injection sensorless drive system. For the estimation of the rotor position, θ_r, the position error signal, $\tilde{\theta}_{r,est}$, is extracted from q-

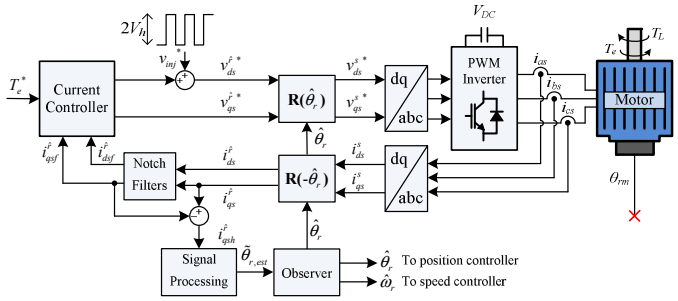

Fig. 1. Square-wave injection sensorless drive system.

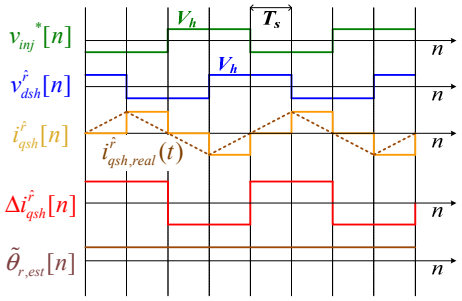

Fig. 2. Procedure of extracting position error signal.

axis current ripple and is inputted to the observer which finally outputs the estimated rotor position, $\hat{\theta}_r$.

This position estimation algorithm is based on the model of IPMSM. The basic model of IPMSM in the rotor reference frame is given by (1).

$$\mathbf{v}_{\mathbf{dqs}}^{\mathbf{r}} = \begin{bmatrix} v_{ds}^r \\ v_{qs}^r \end{bmatrix} = \begin{bmatrix} R_s + pL_{ds} & -\omega_r L_{qs} \\ \omega_r L_{ds} & R_s + pL_{qs} \end{bmatrix} \begin{bmatrix} i_{ds}^r \\ i_{qs}^r \end{bmatrix} + \begin{bmatrix} 0 \\ \omega_r \lambda_f \end{bmatrix}, \tag{1}$$

where v indicates voltage, i current, λ_f flux linkage from permanent magnet, R resistance, L inductance, ω_r rotational speed, superscript 'r' the rotor reference frame, and p differential operator. In HF range, the machine can be seen as an inductive load, which is explained in (2).

$$\mathbf{v}_{\mathbf{dqsh}}^{\mathbf{r}} = \begin{bmatrix} v_{dsh}^r \\ v_{qsh}^r \end{bmatrix} = \begin{bmatrix} pL_{dsh} & 0 \\ 0 & pL_{qsh} \end{bmatrix} \begin{bmatrix} i_{dsh}^r \\ i_{qsh}^r \end{bmatrix}, \tag{2}$$

where subscript 'h' comes from 'high frequency'. As shown in Fig. 1, voltage signal is injected at estimated d-axis. Eq. (3) shows the HF component of voltage reference in a discretized form.

$$\mathbf{v}_{\mathbf{dqsh}}^{\hat{\mathbf{r}}\,*}[n] = \begin{bmatrix} v_{dsh}^{\hat{r}\,*}[n] \\ v_{qsh}^{\hat{r}\,*}[n] \end{bmatrix} = \begin{bmatrix} v_{inj}^{\,*}[n] \\ 0 \end{bmatrix}, \tag{3}$$

where $v_{inj}^{\,*}[n] = \begin{cases} V_h & \text{half duty} \\ -V_h & \text{otherwise} \end{cases}$ and the variables with superscript '*' mean reference values. Considering output delay of digital controller, HF injection voltage in the real rotor reference frame, $\mathbf{v}_{\mathbf{dqsh}}^{\mathbf{r}}[n]$, can be deduced as (4).

$$\mathbf{v}_{\mathbf{dqsh}}^{\mathbf{r}}[n] = \mathbf{R}(-\tilde{\theta}_r) \cdot \mathbf{v}_{\mathbf{dqsh}}^{\hat{\mathbf{r}}\,*}[n-1] = \begin{bmatrix} \cos\tilde{\theta}_r \\ -\sin\tilde{\theta}_r \end{bmatrix} \cdot v_{inj}^{\,*}[n-1], \tag{4}$$

where $\mathrm{R}(\theta)$ indicates rotational transformation defined as (5).

$$\mathbf{R}(\theta) \triangleq \begin{bmatrix} \cos\theta & -\sin\theta \\ \sin\theta & \cos\theta \end{bmatrix}. \tag{5}$$

In (4), $\mathbf{v}_{\mathbf{dqsh}}^{\mathbf{r}}[n]$ means the average value of input voltage between n and n+1 sampling instants. $\tilde{\theta}_r$ is the position error defined as $\tilde{\theta}_r = \theta_r - \hat{\theta}_r$. Then it can be thought that the current variation at n sampling instant, $\Delta\mathbf{i}_{\mathbf{dqsh}}^{\mathbf{r}}[n] = \mathbf{i}_{\mathbf{dqsh}}^{\mathbf{r}}[n] - \mathbf{i}_{\mathbf{dqsh}}^{\mathbf{r}}[n-1]$, is induced by $\mathbf{v}_{\mathbf{dqsh}}^{\mathbf{r}}[n-1]$. From this idea, the current variation in estimated rotor reference frame can be calculated by (6), where T_s indicates sampling period and $\Delta L_{sh} = (L_{dsh} - L_{qsh})/2$.

$$\begin{aligned} \Delta\mathbf{i}_{\mathbf{dqsh}}^{\hat{\mathbf{r}}}[n] &= \mathbf{R}(\tilde{\theta}_r) \cdot T_s \begin{bmatrix} L_{dsh} & 0 \\ 0 & L_{qsh} \end{bmatrix}^{-1} \mathbf{v}_{\mathbf{dqsh}}^{\mathbf{r}}[n-1] \\ &\approx T_s \begin{bmatrix} \left(\frac{1}{L_{dsh}} \cos^2\tilde{\theta}_r + \frac{1}{L_{qsh}} \sin^2\tilde{\theta}_r \right) \\ \left(-\frac{\Delta L_{sh}}{L_{dsh} L_{qsh}} \sin 2\tilde{\theta}_r \right) \end{bmatrix} \cdot v_{inj}^{\,*}[n-2]. \end{aligned} \tag{6}$$

From q-axis current ripple in (6), the position error signal can be computed by (7).

$$\tilde{\theta}_{r,est}[n] = \Delta i_{qsh}^{\hat{r}}[n] \cdot \left(-\frac{L_{dsh} L_{qsh}}{2T_s \cdot \Delta L_{sh}} \right) \frac{1}{v_{inj}^{\,*}[n-2]} \approx \tilde{\theta}_r, \tag{7}$$

Then, the rotor position and speed can be estimated from the observer shown in Fig. 1. The observer adjusts $\hat{\theta}_r$ in the direction that q-axis current ripple which corresponds to the position estimation error is getting diminished. The overall procedure of the signal processing in (3)-(7) is described in Fig. 2.

III. Position Error Induced by Inverter Nonlinearity

A. Inverter nonlinearity effects

Fig. 3 shows one leg of an inverter feeding x-phase of a motor. In the figure, x indicates an arbitrary phase among a, b, and c. Note that there are naturally parasitic capacitors denoted as C_p which are connected in parallel with IGBTs. Thus, collector-emitter capacitance, C_{ce}, is equal to C_p, i.e., $C_{ce} = C_p$. There are mainly two switching states for an output terminal of an inverter: "high" state where i_{xs} flows through the upper IGBT or diode and "low" state where i_{xs} flows through the lower IGBT or diode. On sequence is defined as a period where the switching state changes from "low" state to "high" state, and off sequence is defined in reverse way. There are mainly two inverter nonlinearity effects that provoke pole voltage error defined as (8).

$$\delta v_{xn}[n] = v_{xn}^{\,*}[n-1] - v_{xn}[n]. \tag{8}$$

In (8), $\delta v_{xn}[n]$ means the average value of the voltage error between n and n+1 sampling instants.

The first inverter nonlinearity effect is voltage drop across a switch. In Fig. 4, one switch that consists of an IGBT and an anti-parallel diode is shown. Assuming that the gate is on, v_{sw} can be expressed as a function of i_{sw}, i.e., $v_{sw}(i_{sw})$, which is normally provided in datasheets of IGBT modules. From given $v_{sw}(i_{sw})$, instantaneous pole voltage error from the voltage drop can be represented as (9).

$$\delta v_{xn\_sw} = \begin{cases} -v_{sw}(-i_{xs}) & \text{for "low" state} \\ v_{sw}(i_{xs}) & \text{for "high" state} \end{cases}. \tag{9}$$

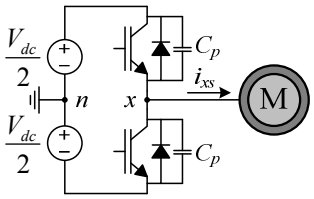

Fig. 3. One leg of an inverter.

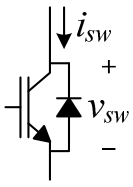

Fig. 4. Voltage drop across a switch.

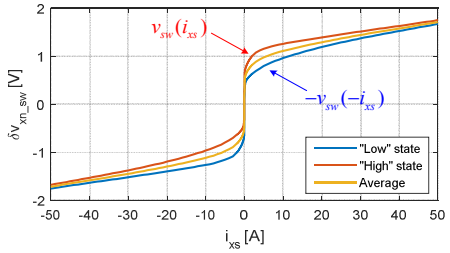

Fig. 5. Pole voltage error from voltage drop across a switch.

Based on (9), the average of δv_{xn_sw} between n and n+1 sampling instants can be expressed as (10).

$$\delta v_{xn\_sw}[n] \approx \frac{T_{high}}{T_s} v_{sw}(i_{xs}[n+0.5]) - \frac{T_{low}}{T_s} v_{sw}(-i_{xs}[n+0.5]), \quad (10)$$

where $i_{xs}[n+0.5] = (i_{xs}[n] + i_{xs}[n+1])/2$ is used as a nominal value of the current. T_{low} and T_{high} indicate "low" and "high" state durations in a sampling period, respectively. Fig. 5 illustrates δv_{xn_sw} according to the current which is extracted from the datasheet of an IGBT module, product number PM50CL1A060. In the figure, the curve with the legend "average" is calculated under the assumption of half duty ratio.

The second inverter nonlinearity effect is the voltage distortion due to the dead time described in Fig. 6. In the figure, the current conduction path at each period is also drawn. During the dead time where both the upper and the lower IGBTs in Fig. 3 are off, i_{xs} can't flow through an IGBT but can flow through a diode or the collector-emitter capacitors of both IGBTs. For this reason, the pole voltage, $v_{xn}(t)$, cannot instantly change in a desired way, which induces the pole voltage error.

To be more specific, i_{xs} flows through a diode during the dead time unless that diode is reverse biased. In this case, $v_{xn}(t)$ is simply delayed by the dead time, T_d, which is shown at on sequence in Fig. 6(a) and off sequence in Fig. 6(b). This delay leads to volt-sec loss or gain denoted as the area A_l or A_g, respectively. In this case, A_l and A_g are equal to $T_d V_{dc}$. At the end of the dead time, the upper/lower IGBT turns on and the output voltage instantly increases/decreases.

In the case that the diode is reverse biased at the start of the dead time, which is shown at off sequence in Fig. 6(a) and on sequence in Fig. 6(b), i_{xs} flows to the parasitic capacitors, charging one capacitor and discharging the other capacitor. In this condition, $v_{xn}(t)$ is neither up-clamped nor down-clamped to the DC link voltage. In this period, the output can be thought as being in a third switching state which will be called as "mid" state in this paper. Assuming that the motor is a current source, $v_{xn}(t)$ linearly increases or decreases with $-i_{xs}/(2C_{ce})$ slope at "mid" state. Volt-sec loss or gain also arises in this period. Fig. 7 shows pole voltage waveform at "mid" state according to the current. In this figure, i_c is a critical value of current defined as (11).

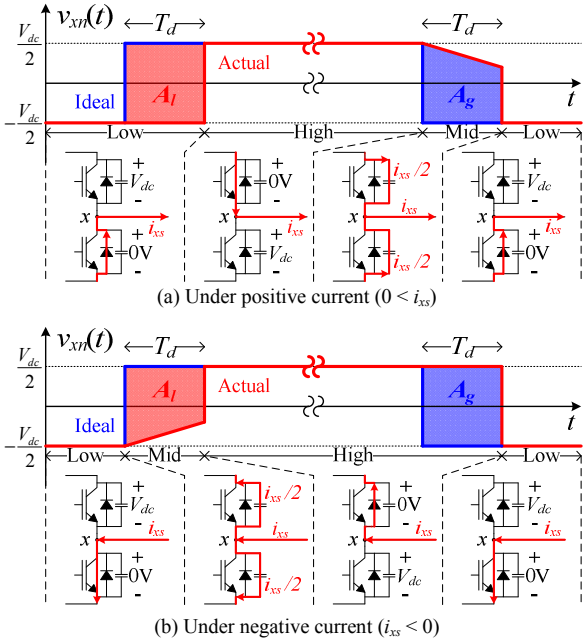

(a) Under positive current ($0 < i_{xs}$)

(b) Under negative current ($i_{xs} < 0$)

Fig. 6. Pole voltage waveforms at on and off sequences. Blue line: ideal pole voltage, red line: actual pole voltage.

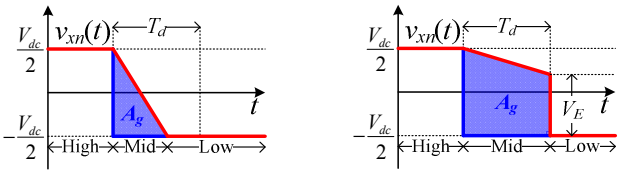

(a) Off Seq., $i_c < i_{xs}$

(b) Off Seq., $0 \le i_{xs} < i_c$

Fig. 7. Pole voltage waveform at "mid" state ($0 \le i_{xs}$).

$$i_c = 2V_{dc} \cdot C_{ce} / T_d . \quad (11)$$

When i_{xs} larger than i_c flows, which is the case of Fig. 7(a), $v_{xn}(t)$ rapidly decrease and clamped to $-V_{dc}/2$. Then the switching state changes to "low" state and i_{xs} starts to flow through the lower diode. When i_{xs} is smaller than i_c and larger than zero, which is the case of Fig. 7(b), $v_{xn}(t)$ is not clamped to $-V_{dc}/2$ during the dead time. In this case, when the dead time ends, the upper capacitor and the lower capacitor are instantly charged and discharged, respectively.

From the above analyses, Eq. (12)-(13) summarize the average pole voltage errors at on and off sequences.

$$\delta v_{xn\_DT\_On}[n] = \frac{A_l}{T_s} = \begin{cases} -\frac{C_{ce}V_{dc}^2}{T_s}\frac{1}{i_{xs\_S}[n]} & (i_{xs\_S}[n] < -i_c) \\ \frac{T_d}{T_s}\left(V_{dc} + \frac{T_d}{4C_{ce}} i_{xs\_S}[n]\right) & (-i_c \le i_{xs\_S}[n] < 0) \\ \frac{T_d}{T_s} V_{dc} & (0 \le i_{xs\_S}[n]) \end{cases} . \quad (12)$$

$$\delta v_{xn\_DT\_Off}[n] = -\frac{A_g}{T_s} = \begin{cases} -\frac{T_d}{T_s} V_{dc} & (i_{xs\_S}[n] < 0) \\ -\frac{T_d}{T_s}\left(V_{dc} - \frac{T_d}{4C_{ce}} i_{xs\_S}[n]\right) & (0 \le i_{xs\_S}[n] < i_c) \\ -\frac{C_{ce}V_{dc}^2}{T_s}\frac{1}{i_{xs\_S}[n]} & (i_c \le i_{xs\_S}[n]) \end{cases} . \quad (13)$$

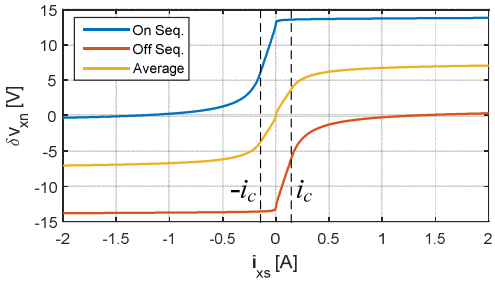

Fig. 8. δv_{xn} according to i_{xs} (C_{ce} = 0.5 nF).

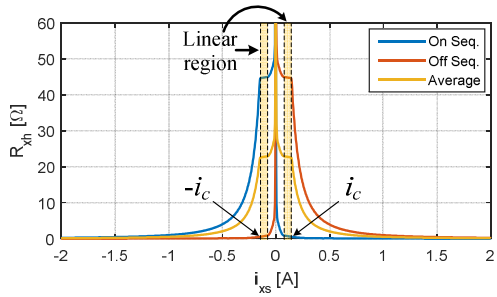

Fig. 9. R_{xh} according to phase current (C_{ce} = 0.5 nF).

Note that $i_{xs\_S}[n]$ in (12)-(13) indicates x-phase current at exact switching instant of x-phase between n and n+1 sampling instants. Since it is very difficult to acquire $i_{xs\_S}[n]$, $i_{xs}[n+0.5]$ will be used instead of $i_{xs\_S}[n]$ hereafter.

Total voltage error is a sum of the voltage errors from the two main sources, as shown in (14).

$$\delta v_{xn}[n] = \delta v_{xn\_sw}[n] + \begin{cases} \delta v_{xn\_DT\_On}[n], & \text{on sequence} \\ \delta v_{xn\_DT\_Off}[n], & \text{off sequence} \end{cases} . \quad (14)$$

$\delta v_{xn}[n]$ according to the phase current calculated from (14) with V_{dc}=310 V, T_d=2 μs, and C_p=0.5 nF is shown in Fig. 8. $\delta v_{xn}[n]$ is affected by both the switching sequences and the phase current. In normal operating condition where the current slowly varies, it would be reasonable to ignore the sequential variation of $\delta v_{xn}[n]$ in Fig. 8. The switching sequences could also be ignored under the signal injection sensorless control if the injection frequency, f_h, is much lower than the switching frequency, f_{sw}, e.g. in the case of sinusoidal voltage injection [2]-[5] with $f_h < 0.2 \cdot f_{sw}$, because the sequential variation of δv_{xn} can be filtered out during the signal processing. However, as f_h increases, the sequential variation of δv_{xn} is not filtered out but reflected to the position error signal. Under the square-wave injection where f_h equals to $0.5 \cdot f_{sw}$ or f_{sw}, the sequential variation of δv_{xn} should definitely be taken into consideration.

B. Influence of Inverter Nonlinearity on Position Estimation

$\delta v_{xn}[n]$ can be divided into fundamental and HF components which are denoted as $\delta v_{xnf}[n]$ and $\delta v_{xnh}[n]$, respectively. Then $\mathbf{\delta v}_{\mathbf{abcn}}[n]$ can be expressed as (15).

$$\mathbf{\delta v}_{\mathbf{abcn}}[n] = \mathbf{\delta v}_{\mathbf{abcnf}}[n] + \mathbf{\delta v}_{\mathbf{abcnh}}[n] , \quad (15)$$

where $\mathbf{\delta v}_{\mathbf{abcn}}[n] \triangleq \left[\delta v_{an}[n] \quad \delta v_{bn}[n] \quad \delta v_{cn}[n]\right]^T$, and $\mathbf{\delta v}_{\mathbf{abcnf}}[n]$ and $\mathbf{\delta v}_{\mathbf{abcnh}}[n]$ are defined in similar ways. In (15), $\mathbf{\delta v}_{\mathbf{abcnf}}[n]$ doesn't affect the sensorless control since it is normally filtered out during the signal processing. In other words, only $\mathbf{\delta v}_{\mathbf{abcnh}}[n]$ affects the signal injection sensorless control. Thus it is needed to analyze how $\mathbf{\delta v}_{\mathbf{abcnh}}[n]$ affects the sensorless control.

Introducing a concept of HF resistance, $\mathbf{\delta v}_{\mathbf{abcnh}}[n]$ can be expressed as (16).

$$\mathbf{\delta v}_{\mathbf{abcnh}}[n] \approx \begin{bmatrix} R_{ah} & 0 & 0 \\ 0 & R_{bh} & 0 \\ 0 & 0 & R_{ch} \end{bmatrix} \begin{bmatrix} i_{ash}[n+0.5] \\ i_{bsh}[n+0.5] \\ i_{csh}[n+0.5] \end{bmatrix} , \quad (16)$$

where R_{xh} is defined as $R_{xh} \triangleq \dfrac{d}{di_{xs}} \delta v_{xn}$. In Fig. 9, R_{xsh} according to i_{xs} is derived simply by differentiating δv_{xn} in Fig. 8. Since R_{xh} varies according to i_{xs}, the resistance matrix in (16) can be understood as a three-phase unbalanced resistive load. The peaking of R_{xh} at zero current in Fig. 9 is an unavoidable phenomenon since it comes from high slope of $\delta v_{xn\_sw}[n]$ at $i_{xs} = 0$ in Fig. 5. Just aside the peak, there is a narrow flat-top region between $-i_c$ and i_c which is denoted as linear region. As specified in (12)-(13), R_{xh} has a constant value determined by C_{ce} in the linear region.

Using dq transformation matrix defined as (17), $\mathbf{\delta v}_{\mathbf{abcnh}}[n]$ can be transformed into the stationary dq coordinate plane as (18).

$$\mathbf{T}_{\mathbf{dq}} \triangleq \frac{2}{3} \begin{bmatrix} 1 & -1/2 & -1/2 \\ 0 & \sqrt{3}/2 & -\sqrt{3}/2 \end{bmatrix} . \quad (17)$$

$$\mathbf{\delta v}^{\mathbf{s}}_{\mathbf{dqsh}}[n] = \begin{bmatrix} \delta v^s_{dsh} \\ \delta v^s_{qsh} \end{bmatrix} = \mathbf{T}_{\mathbf{dq}} \cdot \mathbf{\delta v}_{\mathbf{abcnh}}[n] = \begin{bmatrix} R^s_{dh} & R^s_{dqh} \\ R^s_{qdh} & R^s_{qh} \end{bmatrix} \begin{bmatrix} i^s_{dsh}[n+0.5] \\ i^s_{qsh}[n+0.5] \end{bmatrix} , \quad (18)$$

where the four resistances are $R^s_{dh} = 1/6 \cdot (4R_{ah} + R_{bh} + R_{ch})$, $R^s_{qh} = 1/2 \cdot (R_{bh} + R_{ch})$, and $R^s_{dqh} = R^s_{qdh} = \sqrt{3}/6 \cdot (R_{ch} - R_{bh})$. Due to the unbalanced three-phase resistances, R^s_{dh} and R^s_{qh} are different and there are off-diagonal components in the resistance matrix in (18). It can be thought as a stator-oriented resistance saliency.

Transforming $\mathbf{\delta v}^{\mathbf{s}}_{\mathbf{dqsh}}[n]$ into the estimated rotor reference frame, (19) can be derived.

$$\begin{aligned} \mathbf{\delta v}^{\hat{\mathbf{r}}}_{\mathbf{dqsh}}[n] &= \mathbf{R}(-\hat{\theta}_r) \cdot \mathbf{\delta v}^{\mathbf{s}}_{\mathbf{dqsh}}[n] \\ &= \begin{bmatrix} \Sigma R_h - R_{mh}\cos\left(2\hat{\theta}_r + \phi\right) & R_{mh}\sin\left(2\hat{\theta}_r + \phi\right) \\ R_{mh}\sin\left(2\hat{\theta}_r + \phi\right) & \Sigma R_h + R_{mh}\cos\left(2\hat{\theta}_r + \phi\right) \end{bmatrix} \begin{bmatrix} i^{\hat{r}}_{dsh}[n+0.5] \\ i^{\hat{r}}_{qsh}[n+0.5] \end{bmatrix} , \end{aligned} \quad (19)$$

where $R_{mh} \triangleq \sqrt{{R^s_{dqh}}^2 + \left(R^s_{dh} - R^s_{qh}\right)^2 / 4}$, $\Sigma R_h \triangleq \dfrac{R^s_{dh} + R^s_{qh}}{2}$, and $\phi = -\arctan\left(2R^s_{dqh} / \left(R^s_{dh} - R^s_{qh}\right)\right)$. The resistance matrix seen from the estimated rotor reference frame in (19) is very similar with the inductance matrix seen from the stationary reference frame.

Taking the voltage error in (19) into account in the signal injection sensorless control, the actual injection voltage in (4) is modified to (20).

$$\mathbf{v}^{\mathbf{r}}_{\mathbf{dqsh}}[n] = \mathbf{R}(-\tilde{\theta}_r) \cdot \left(\mathbf{v}^{\hat{\mathbf{r}}}_{\mathbf{dqsh}}{}^*[n-1] - \mathbf{\delta v}^{\hat{\mathbf{r}}}_{\mathbf{dqsh}}[n]\right) . \quad (20)$$

Table I. Parameters of IPMSM.

Rated speed	3000 r/min	λ_f	0.0625 V·s
Rated power	300 W	R_s	1.38 Ω
Rated current	2.85 A_{rms}	L_{ds}	6.9 mH
Pole number	6	L_{qs}	10.6 mH

Then the current ripple equation in (6) can be modified to (21).

$$\Delta \mathbf{i}^{\hat{\mathbf{r}}}_{\mathbf{dqsh}}[n] \approx T_s \begin{bmatrix} \frac{2\Delta L_{sh}}{L_{dsh}L_{qsh}} \cdot \delta v^{\hat{r}}_{qsh}[n-1] \cdot \tilde{\theta}_r + \frac{v_{inj}^{*}[n-2] - \delta v^{\hat{r}}_{dsh}[n-1]}{L_{dsh}} \\ \frac{-2\Delta L_{sh}}{L_{dsh}L_{qsh}} \cdot \left(v_{inj}^{*}[n-2] - \delta v^{\hat{r}}_{dsh}[n-1]\right) \cdot \tilde{\theta}_r - \frac{\delta v^{\hat{r}}_{qsh}[n-1]}{L_{qsh}} \end{bmatrix} \cdot (21)$$

Applying the computation in (7), the position error signal becomes as follows.

$$\tilde{\theta}_{r,est}[n] \approx k_{scale}[n] \cdot \tilde{\theta}_r + d[n], \quad (22)$$

where

$$k_{scale}[n] = 1 - \frac{\delta v^{\hat{r}}_{dsh}[n-1]}{v_{inj}^{*}[n-2]} \text{ and } d[n] = \frac{L_{dsh}}{2\Delta L_{sh}} \frac{\delta v^{\hat{r}}_{qsh}[n-1]}{v_{inj}^{*}[n-2]}. \quad (23)$$

$k_{scale}[n]$ is a scale factor which is mostly affected by $\delta v^{\hat{r}}_{dsh}[n]$. $d[n]$ is a disturbance input which arises from $\delta v^{\hat{r}}_{qsh}[n]$. Ideally, $k_{scale}[n]=1$ and $d[n]=0$ but they cannot be because of $\delta v^{\hat{r}}_{dsh}[n]$ and $\delta v^{\hat{r}}_{qsh}[n]$. $\delta \mathbf{v}^{\hat{\mathbf{r}}}_{\mathbf{dqsh}}[n]$ can be compensated if f_h is much lower than f_{sw} [17]. But such compensation is almost impossible under the square-wave injection where f_h is extremely high because of rapid variation of the current and the digital control delay which is about $1.5T_s$ [18].

To show the effects of the inverter nonlinearity under the signal injection, simulations were carried out. In the first simulation, an IPMSM whose parameters are specified in table I is driven with sensored control, V_h=5V, and zero fundamental current. In this condition, typical waveforms are shown in Fig. 10. In the figure, although $v^{r}_{dsh}{}^{*}[n-1]$ with square shape is applied, actual injection voltage is distorted by $\delta v^{r}_{dsh}[n]$, which causes irregular waveform of $i^{r}_{dsh}[n]$. And there is also $\delta v^{r}_{qsh}[n]$ which causes small $i^{r}_{qsh}[n]$. This small $i^{r}_{qsh}[n]$ which purely comes from the voltage error directly goes to the signal processing in (7) and results in the position error.

In the second simulation, under the same condition as the first one, the effects of the injection voltage on $k_{scale}[n]$ and $d[n]$ are investigated. According to (23), as V_h increases, $k_{scale}[n]$ and

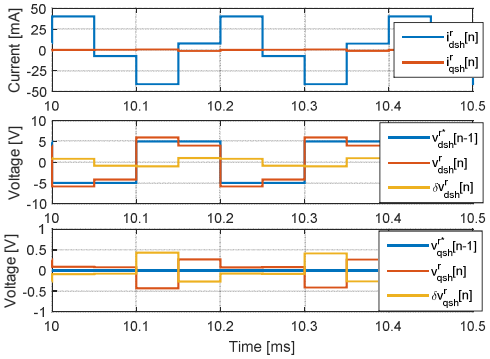

Fig. 10. Simulation 1: Typical current and voltage waveforms.

$d[n]$ become closer to unity and zero, respectively. This tendency is clearly seen in Fig. 11(a)-(b). The fluctuations of $k_{scale}[n]$ and $d[n]$ under V_h = 5 V are remarkably relieved by increasing V_h to 20 V. Although increasing V_h works in improving the performance, it is not a desirable solution practically since side effects such as audible noise and HF loss would be also increased.

IV. Capacitor-Integrated Inverter for Reduced Injection Voltage

The only way to improve the performance under a fixed low V_h is reducing $\delta \mathbf{v}^{\hat{\mathbf{r}}}_{\mathbf{dqsh}}[n]$. In the resistance matrix in (19), there are two resistance terms which are simplified as follows.

$$\Sigma R_h = \frac{1}{3}\left(R_{ah} + R_{bh} + R_{ch}\right). \quad (24)$$

$$R_{mh} = \frac{\sqrt{2}}{6}\sqrt{\left(R_{ah} - R_{bh}\right)^2 + \left(R_{bh} - R_{ch}\right)^2 + \left(R_{ah} - R_{ch}\right)^2}. \quad (25)$$

In (19), ΣR_h forms symmetric resistance and R_{mh} provokes the resistance saliency. Applying HF voltage injection at d-axis, ΣR_h functions as reducing HF current ripple at d-axis, whereas R_{mh} induces additional HF current ripple at q-axis. Therefore ΣR_h and R_{mh} correspond to $\delta v^{\hat{r}}_{dsh}[n]$ and $\delta v^{\hat{r}}_{qsh}[n]$, respectively. In order to decrease $\delta v^{\hat{r}}_{dsh}[n]$, overall magnitudes of the three resistances should be reduced. For decreasing $\delta v^{\hat{r}}_{qsh}[n]$, the three resistances should be close to each other.

From these observations, it can be found that both $\delta v^{\hat{r}}_{dsh}[n]$ and $\delta v^{\hat{r}}_{dsh}[n]$ can be decreased by reducing R_{xh} and expanding the linear region in Fig. 9. And these can be done by simply increasing C_{ce} because i_c and R_{xh} in the linear region are proportional and inversely proportional to C_{ce}, respectively, as

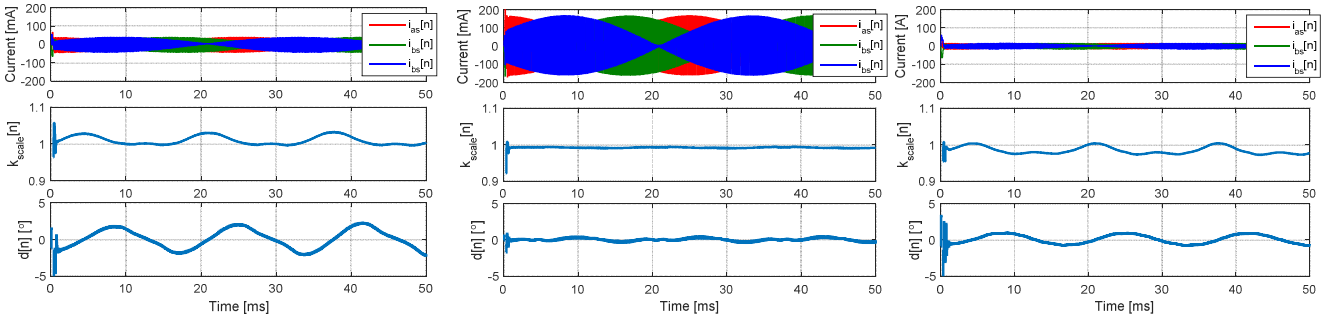

(a) V_h = 5 V, C_{ce} = 0.5 nF (b) V_h = 20 V, C_{ce} = 0.5 nF (c) V_h = 2 V, C_{ce} = 2.7 nF

Fig. 11. Simulation 2: Variations of $k_{scale}[n]$ and $d[n]$.

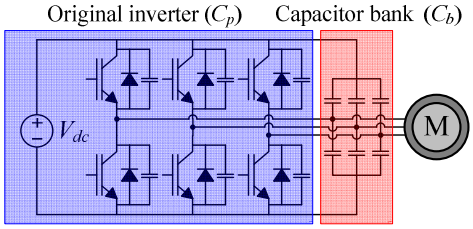

Fig. 12. Capacitor-integrated inverter.

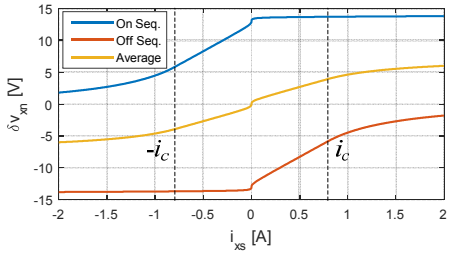

Fig. 13. δv_{xn} according to i_{xs} (C_{ce} = 2.7 nF).

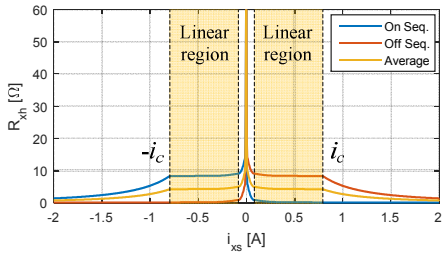

Fig. 14. R_{xh} according to phase current (C_{ce} = 2.7 nF).

written in (11) and (12)-(13). In order to increase C_{ce}, additional capacitors can be connected to the inverter. Fig. 12 shows the proposed capacitor-integrated inverter. As shown in Fig. 12, a capacitor bank containing six capacitors (C_b) is connected to the original inverter. The additional capacitors are linked in parallel with the inherent parasitic capacitors. Thus the effective collector-emitter capacitance can be increased to $C_{ce} = C_p + C_b$. In the connection of the capacitor bank, it should be placed close to the AC output terminals of the inverter and DC link to minimize stray inductances. Then the additional capacitors can also function as snubber capacitors that prevent severe dv/dt of IGBTs resulting in less EMI.

Fig. 13 and 14 illustrate δv_{xn} and R_{xh} according to i_{xs} with C_b=2.2 nF, i.e., C_{ce}=2.7 nF. Comparing Fig. 14 with Fig. 9, overall magnitude of R_{xh} is reduced in Fig. 14, which helps reducing both ΣR_h and R_{mh}. Especially with sinusoidal voltage injection cases [2]-[5] where f_h is much lower than f_{sw}, the average R_{xh} curve in Fig. 14 is effective. Then expanded width of the linear region has a beneficial effect that if the three-phase currents are inside that region, R_{mh} goes to zero since R_{ah}, R_{bh}, and R_{ch} become the same in that region. This in turn reduces $d[n]$, which is very helpful for the sensorless control in no load condition.

In Fig. 11(c), simulation waveforms of $k_{scale}[n]$ and $d[n]$ with V_h=2 V and C_{ce}=2.7 nF are depicted. Comparing Fig. 11(c) with (a), it is worth noting that although V_h is decreased by 60% in Fig. 11 (c), the characteristics of $k_{scale}[n]$ and $d[n]$ are even better thanks to the positive effects of increasing C_{ce}.

Fig. 15 shows simulation results under the sensorless current control, the speed held at 400 r/min, no load. V_h and C_{ce} are written in the caption of the figure. Although V_h is much lower in

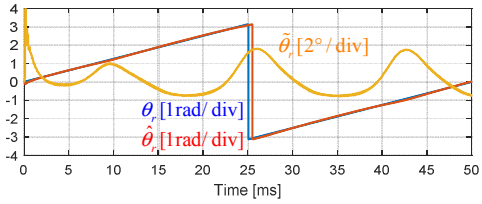

(a) V_h = 5 V, C_{ce} = 0.5 nF

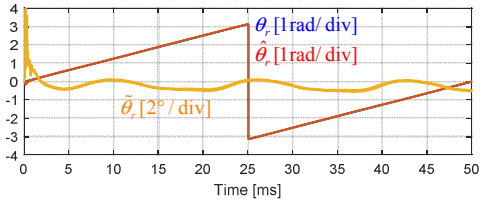

(b) V_h = 2 V, C_{ce} = 2.7 nF

Fig. 15. Simulation 3: Sensorless control performance.

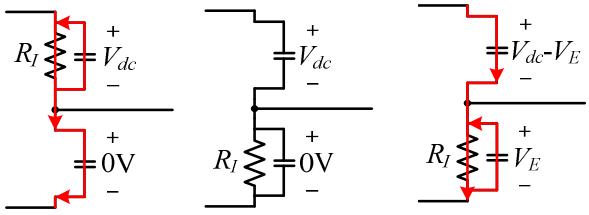

(a) On Seq., $0 \le i_{xs}$ (b) Off Seq., $i_c < i_{xs}$ (c) Off Seq., $0 \le i_{xs} < i_c$

Fig. 16. Current conduction paths at the end of the dead time. ($0 \le i_{xs}$)

Fig. 15(b), the peak-to-peak value of the position error is 1.14° whereas that is 5.04° in Fig. 15(a). This means that using the capacitor-integrated inverter, the injection can be reduced without degrading the sensorless control performance.

One of side effects coming from the connected capacitors is increased switching loss. Fig. 16 illustrates current conduction paths at the end of the dead time with positive current. At on sequence, the upper capacitor is charged with V_{dc} and the lower one is fully discharged. At the end of the dead time where the upper IGBT turns on, the equivalent cirquit can be derived as Fig. 16(a). The closed IGBT forms a current conduction path with very low resistance, R_I, discharging the upper capacitor and charging the lower capacitor in the same time. The energy stored in the upper capacitor, $1/2 \cdot C_{ce}V_{dc}^2$, is comsumed in R_I. In the same time, while charging the lower capacitor, an energy amounts to $1/2 \cdot C_{ce}V_{dc}^2$ is also consumed in R_I. Therefore, total energy loss at on sequence is $C_{ce}V_{dc}^2$. At off sequence, when i_{xs} is larger than i_c, the upper/lower capacitor is already fully charged/dischraged at the end of the dead time. There isn't any loss in this condition. At off sequence, when i_{xs} is between zero and i_c, the lower capacitor is not fully discharged but contains V_E as shown in Fig. 7(b). In this condition, total energy loss is $C_{ce}V_E^2$.

In this way, instantaneous power loss coming from the capacitors including the additional capcitors in x-phase arm of an inverter can be expressed as (26).

$$P_{Cx}(i_{xs}) = \begin{cases} C_{ce}V_{dc}^2 f_{sw} & (i_{xs} < -i_c) \\ C_{ce}\left(\frac{T_d^2}{4C_{ce}^2} i_{xs}^2 + \frac{T_d V_{dc}}{C_{ce}} i_{xs} + 2V_{dc}^2\right) f_{sw} & (-i_c \le i_{xs} < 0) \\ C_{ce}\left(\frac{T_d^2}{4C_{ce}^2} i_{xs}^2 - \frac{T_d V_{dc}}{C_{ce}} i_{xs} + 2V_{dc}^2\right) f_{sw} & (0 \le i_{xs} < i_c) \\ C_{ce}V_{dc}^2 f_{sw} & (i_c \le i_{xs}) \end{cases} . \quad (26)$$

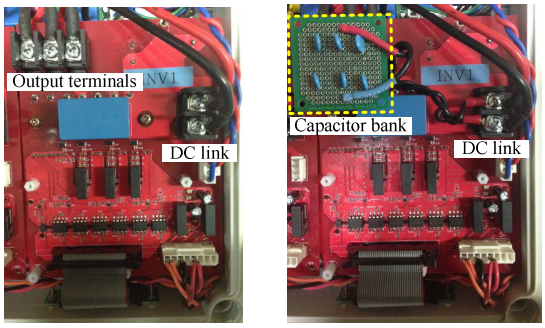

(a) Original inverter (b) Capacitor-integrated inverter

Fig. 17. Experimental implementation of capacitor-integrated inverter.

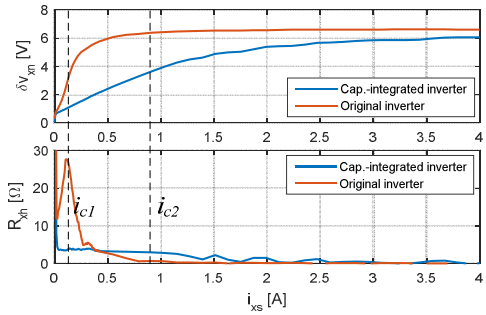

Fig. 18. Experiment 1: Measurement of δv_{xn} and R_{xh}.

Assuming that three-phase balanced currents with the magnitude I_1 are flowing, the average power loss of the inverter can be deduced as (27).

$$P_{C\text{avg}} = 3f_1\int_0^{1/f_1} P_{Cx}(I_1\cos 2\pi f_1 t)dt\ . \tag{27}$$

The analytic solution of $P_{C\text{avg}}$ in (27) is not provided in this paper because it is over-complicated due to trigonometric functions. But it can be found from (26) that $P_{C\text{avg}}$ can be approximated to $3C_{ce}V_{dc}{}^2 f_{sw}$ with $i_c \ll I_1$ or to $6C_{ce}V_{dc}{}^2 f_{sw}$ with zero fundamental current. In any case, $P_{C\text{avg}}$ is directly proportional to C_{ce}. Therefore, in the determination of C_{ce}, the trade-off relation between the performance and the loss should be considered. In the case of an IPMSM drive system with machine parameters in table I, C_b =2.2nF, f_{sw}=10 kHz, and V_{dc}=118 V which is optimized to the machine's rated condition, the loss coming from the additional capacitors is 919mW in the rated condition. This loss is only 0.3% of the machine's power rating, i.e., 300W.

V. Experimental Resutls

Fig. 17 shows experimental implementation of the capacitor-integrated inverter. In Fig. 17(a), the original inverter and its drive circuits are implemented on a PCB. In Fig. 17(b), a capacitor bank containing six ceramic capacitors with C_b =2.2 nF is connected to the inverter in the way described in Fig. 12. To minimize stray inductances, the capacitor bank is put directly on the output terminals and DC link cables are twisted. This hardware implementation can be improved by including the additional capacitors in the PCB with the IGBT module. The output of the inverter is connected to an IPMSM whose parameters are specified in table I. The switching frequency is 10 kHz, T_s = 50 μs, T_d = 2 μs, and V_{dc}=310 V.

Fig. 18 shows experimentally measured δv_{xn} and R_{xh} before and after connecting the capacitor bank. In the experiment, only

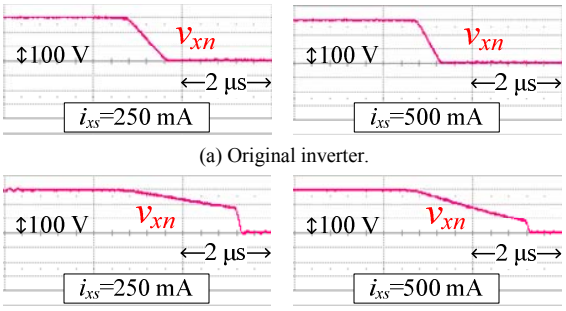

(a) Original inverter.

(b) Capacitor-integrated inverter.

Fig. 19. Experiment 2: Waveform of pole voltage at off sequence.

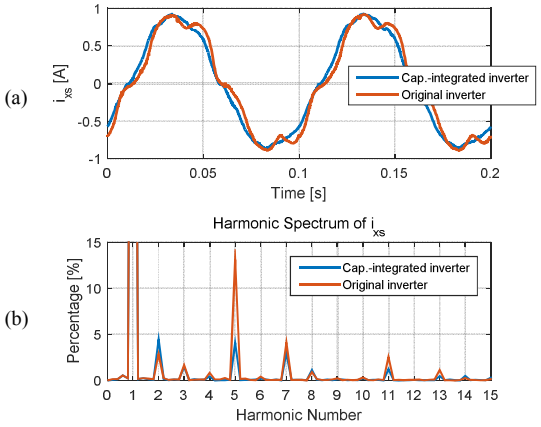

Fig. 20. Experiment 3: (a) Current waveform and (b) its harmonic spectrum.

average value of δv_{xn} is measured. The experimental data clearly show that the linear region is expanded by the additional capacitors. The dipping of R_{xh} aside the peak in the original inverter case comes from that C_p is not a constant value but varies according to the collector-emitter voltage.

In Fig. 19, pole voltage waveforms with positive current at off sequence where capacitive charging/discharging occurs are shown. This experimental result shows that due to increased C_{ce}, the pole voltage decreases much slower under the same current using the capacitor-integrated inverter.

In Fig. 20, current waveforms with the two inverters are shown. In this experiment, sinusoidal voltage references are applied to the inverter without current regulation to clearly show the inverter nonlinearity effects. By adjusting the magnitude of the voltage reference, the fundamental current magnitudes of the two inverters are set to 0.8A, which is i_c of the capacitor-integrated inverter. As shown in Fig. 20, the current waveform in the proposed inverter case is much better thanks to the widen linear region depicted in Fig. 18. Using the proposed inverter, the inverter nonlinearity simply functions as increasing the resistance of the IPMSM, which rarely causes harmonic distortion of the current.

In this experiment, sensorless control under current regulation is performed with the two inverters. The speed is held at 200 r/min by load machine. In Fig. 21(a), using the original inverter, V_h is abruptly changed from 6V to 5V during the sensorless control. After reducing V_h, the position error begins to increase and finally the rotor position information is lost. However, using the capacitor-integrated inverter, the sensorless operation is stable even with V_h=3V thanks to reduced voltage error.

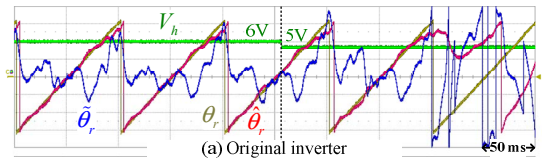

(a) 6V → 5 V square wave injection with original inverter

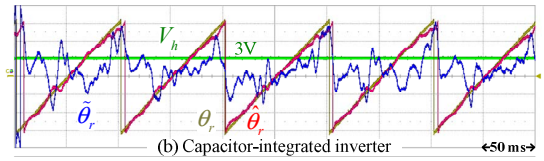

(b) 3 V square wave injection with capacitor-integrated inverter

Fig. 21. Experiment 4: Sensorless control with current regulation. (θ_r :[1rad/ div] , $\hat{\theta}_r$:[1rad/ div] , $\tilde{\theta}_r$:[10° / div] , V_h :[3 V/ div])

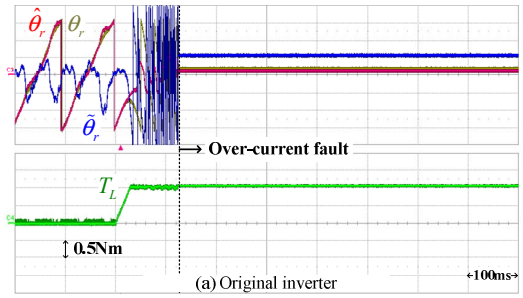

(a) 5 V square wave injection with original inverter

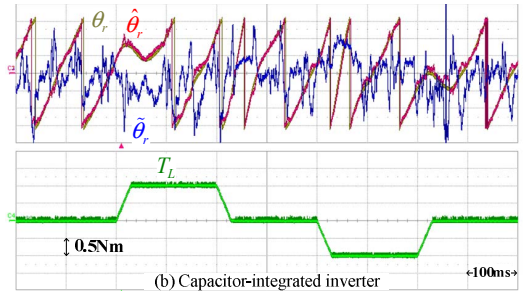

(b) 2 V square wave injection with capacitor-integrated inverter

Fig. 22. Experiment 5: Sensorless control with speed regulation.

(θ_r :[1rad/ div] , $\hat{\theta}_r$:[1rad/ div] , $\tilde{\theta}_r$:[10° / div])

Fig. 22 shows the sensorless control performance while the target machine is regulating the speed at 600 r/min. Meanwhile, varying load torque, T_L, with 20 p.u./s slew rate is applied by the load machine. In case of original inverter and 5V injection, the controller fails to retain the position information and stops due to over-current fault. However, with the capacitor-integrated inverter, the controller withstands the load torque disturbance even with much smaller injection voltage, V_h=2V.

VI. Conclusions

In this paper, the effects of the inverter nonlinearity on the signal injection sensorless control are analyzed. In the analysis, it is revealed that the position estimation performance is degraded especially with injection voltage. In order to reduce the injection voltage without degrading the sensorless control performance, the capacitor-integrated inverter has been proposed. In the proposed inverter, increased collector-emitter capacitance makes the inverter more linear and helps to enhance the performance of the position estimation as the result. Experimental results clearly show that the injection voltage can be reduced to less than a half, still maintaining the reasonable performance of the sensorless control.

References

[1] M. Schroedl, "Sensorless control of AC machines at low speed and standstill based on "INFORM" method," in *Conf. Rec. IEEE-IAS Annu. Meeting*, vol. 1, 1996, pp. 270-277.

[2] P. L. Jansen and R. D. Lorenz, "Transducerless position and velocity estimation in induction and salient ac machines," *IEEE Trans. Ind. Appl.*, vol. 31, no. 2, pp. 240–247, Mar./Apr. 1995.

[3] J. I. Ha, and S. K. Sul, "Sensorless field-orientation control of an induction machine by high-frequency signal injection," *IEEE Trans. Ind. Appl.*, vol. 35, no. 1, pp. 45-51, Jan./Feb. 1999.

[4] J. H. Jang, S. K. Sul, J. I. Ha, K. Ide, and M. Sawamura, "Sensorless drive of surface-mounted permanent-magnet motor by high-frequency signal injection based on magnetic saliency," *IEEE Trans. Ind. Appl.*, vol. 39, no. 4, pp. 1031-1039, Jul./Aug. 2003.

[5] S. C. Yang and R. D. Lorenz, "Surface permanent magnet synchron-ous machine position estimation at low speed using eddy-current-reflected asymmetric resistance," *IEEE Trans. Power Electron.*, vol. 27, no. 5, pp. 2595–2604, May 2012.

[6] Y. D. Yoon, S. K. Sul, S. Morimoto, and K. Ide, "High bandwidth sensorless algorithm for AC machines based on square-wave-type voltage injection," *IEEE Trans. Ind. Appl.*, vol. 47, no. 3, pp. 1361-1370, May/Jun. 2011.

[7] S. Kim, J. I. Ha, and S. K. Sul, "PWM switching frequency signal injection sensorless method in IPMSM," *IEEE Trans. Ind. Appl.*, vol. 48, no. 5, pp. 1576-1587, Sept./Oct. 2012.

[8] Y. Murai, A. Riyanto, H. Nakamura, and K. Matsui, "PWM strategy for high frequency carrier inverters eliminating current-clamps during switching dead-time," in *Conf. Rec. IEEE-IAS Annu. Meeting*, Houston, TX, 1992, pp. 317–322.

[9] J. W. Choi and S. K. Sul, "A new compensation strategy reducing voltage/current distortion in PWM VSI systems operating with low output voltages," *IEEE Trans. Ind. Appl.*, vol. 31, no. 5, pp. 1001–1008, Sept./Oct. 1995.

[10] J. S. Kim, J. W. Choi, and S. K. Sul, "Analysis and compensation of voltage distortion by zero current clamping in voltage-fed PWM inverter," in *Proc. IPEC'95 Conf.*, Yokohama, Japan, Apr. 3–7, 1995, pp. 265–270.

[11] J. W. Choi and S. K. Sul, "Inverter output voltage synthesis using novel dead time compensation," *IEEE Trans. Power Electron.*, vol. 11, no. 2, pp. 221–227, Mar. 1996.

[12] H. S. Kim, H. T. Moon, and M. J. Youn, "On-line dead-time compensation method using disturbance observer," *IEEE Trans. Power Electron.*, vol. 18, no. 6, pp. 1336–1345, Nov. 2003.

[13] G. Pellegrino, R. I. Bojoi, P. Guglielmi, and F. Cupertino, "Accurate inverter error compensation and related self-commissioning scheme in sensorless induction motor drives," *IEEE Trans. Ind. Appl.*, vol. 46, no. 5, pp. 1970–1978, Sep./Oct. 2010.

[14] Y. Park and S. K. Sul, "A novel method utilizing trapezoidal voltage to compensate for inverter nonlinearity," *IEEE Trans. Power Electron.*, vol. 27, no. 12, pp. 4837–4846, Dec. 2012.

[15] J. M. Guerrero, M. Leetmaa, F. Briz, A. Zamarron, and R. D. Lorenz, "Inverter nonlinearity effects in high-frequency signal-injection-based sensorless control methods," *IEEE Trans. Ind. Appl.*, vol. 41, no. 2, pp. 618–626, Mar./Apr. 2005.

[16] K. Wiedmann, F. Wallrapp, and A. Mertens, "Analysis of inverter nonlinearity effects on sensorless control for permanent magnet machine drives based on high-frequency signal injection," in *Proc. 13th Eur. Conf. Power Electron. Appl.* (EPE), 2009, pp. 1–10.

[17] C. H. Choi and J. K. Seok, "Compensation of zero-current clamping effects in high-frequency-signal-injection-based sensorless PM motor drives," *IEEE Trans. Ind. Appl.*, vol. 43, no. 5, pp. 1258–1265, Sept./Oct. 2007.

[18] D. Kim, Y. C. Kwon, S. K. Sul, J. H. Kim, and R. S. Yu, "Suppression of injection voltage disturbance for high frequency square-wave injection sensorless drive with regulation of induced high frequency current ripple," in *IPEC-Hiroshima 2014*, pp.925-932.